Applied Catalysis B: Environmental 242 (2019) 85–91

Contents lists available at ScienceDirect

Applied Catalysis B: Environmental

journal homepage: www.elsevier.com/locate/apcatb

Electrocatalysis of 5-hydroxymethylfurfural at cobalt based spinel catalysts with filamentous nanoarchitecture in alkaline media

Myung Jong Kang[a,1], Heesun Park[b,1], Jonggeon Jegal[b], Sung Yeon Hwang[b,c,**], Young Soo Kang[a,*], Hyun Gil Cha[b,*]

[a] Korea Center for Artificial Photosynthesis, Department of Chemistry, Sogang University, Seoul, 04107, Republic of Korea
[b] Research Center for Bio-based Chemistry, Korea Research Institute of Chemical Technology, Ulsan, 44412, Republic of Korea
[c] Advanced Materials and Chemical Engineering, University of Science and Technology (UST), Daejeon, 34113, Republic of Korea

ARTICLE INFO

Keywords:
Spinel structure
5-Hydroxylmethylfurfural
Electrocatalysis
2,5-Furandicarboxylic acid

ABSTRACT

This study reports the activity of cobalt based metal oxide electrode with spinel structure for 5-hydroxymethylfurfural (HMF) oxidation. For that purpose, the Co_3O_4 and $NiCo_2O_4$ electrode with filamentous nanoarchitecture were grown on Ni foam by a hydrothermal method and then characterized by means of SEM, TEM, and XPS analyses. During electrochemical oxidation of HMF, the role of Co^{3+} in Co_3O_4 and $NiCo_2O_4$ spinel structure was investigated by XANES. The filamentous nanoarchitecture of $NiCo_2O_4$ showed 99.6% 5-hydroxymethylfurfural (HMF) conversion efficiency with 90.8% selectivity on 2,5-furandicarboxylic acid (FDCA). The catalyst was successfully recycled up to three times, retaining over 80% of FDCA conversion efficiency. These results demonstrated the potential interest of $NiCo_2O_4$ anodic catalyst, prepared via hydrothermal method, for production of high-valued chemical from biomass-derived compounds via electrochemical techniques.

1. Introduction

With the increasing demand for renewable and sustainable energy sources, the production of clean fuels and replacement of petroleum-based carbon sources for synthesizing chemicals and materials have become important [1,2]. Biomass, a sustainable source of energy developed from organic materials, is the only renewable non-petroleum-based carbon source [3–5]. The carbon sources stored in organic materials can be utilized as fuels and chemicals through the bio-refinery process [6]. Among the biomass-derived intermediates for bio-refineries, 5-hydroxymethylfurfural (HMF) [7], one of the furan based compounds, is regarded as the most important precursor chemical for the production of plastics, liquid fuels and pharmaceuticals. Polyamides, polyesters, and polyurethanes can be prepared from 2,5-furandicarboxylic acid (FDCA), one of the oxidized forms of HMF, instead of petroleum-derived terephthalic acid [8,9]. Therefore, conversion of HMF to FDCA is regarded as the key process for the biomass refinery process and most studies are focused on this process.

The limitations in the previous reports on the HMF oxidation to FDCA are that the suggested oxidation system requires high temperature and high pressure of O_2 with noble metal-based catalysts such as Pt, Pd, Au or their alloys [10–15] and several less-valued products such as 2,5-diformylfuran (DFF), 5-hydroxymethyl-2-furancarboxylic acid (HMFCA), and 5-formylfuran-2-carboxylic acid (FFCA) are formed [16–18]. Some kinds of supported Au-based catalysts (Au/TiO_2 [11], Au/CeO_2 [19], etc.) and Pt- based catalysts (Pt/C [20], Pt/ZrO_2 [21], etc.) require excessive alkalinity with NaOH or Na_2CO_3, while the electrocatalytic oxidation of HMF is driven by electricity under atmospheric and room temperature conditions. However, very few electrocatalytic systems for HMF oxidation to FDCA have been reported due to the problems of employing a redox mediator (TEMPO) during reaction and precious metal as electrodes [22].

Herein, we report non-precious metal-based electrodes for HMF oxidation to FDCA without employing a redox mediator. The characteristics and performance of the electrochemical oxidation of HMF to FDCA in an aqueous phase with filamentous nanoarchitectured Co_3O_4 and $NiCo_2O_4$ on Ni foam, maintaining high electrocatalytic efficiency and recyclability is reported.

* Corresponding authors.
** Corresponding author at: Research Center for Bio-based Chemistry, Korea Research Institute of Chemical Technology, Ulsan, 44412, Republic of Korea/ Advanced Materials and Chemical Engineering, University of Science and Technology (UST), Daejeon, 34113, Republic of Korea
E-mail addresses: crew75@krict.re.kr (S.Y. Hwang), yskang@sogang.ac.kr (Y.S. Kang), hgcha@krict.re.kr (H.G. Cha).
[1] These authors contributed equally to this work.

https://doi.org/10.1016/j.apcatb.2018.09.087
Received 21 February 2018; Received in revised form 19 September 2018; Accepted 27 September 2018
Available online 01 October 2018

2. Experimental

2.1. Chemicals

$Ni(NO_3)_2{\cdot}6H_2O$, $Co(NO_3)_2{\cdot}6H_2O$, ethanol and urea were bought from Sigma-Aldrich Co. Nickel foams were purchased from MTI Corporation. Water was deionized (18 MΩ/cm) with a Millipore Milli-Q Interral 10 system and used in all studies. All chemicals were used as received without further purification.

2.2. Preparation of Co_3O_4 and $NiCo_2O_4$ filamentous nanoarchitectures on Ni foam

The nickel foam (1 cm × 1 cm) was carefully cleaned with 6 M HCl in an ultrasound bath for 30 min in order to remove the NiO layer on the surface, and then rinsed with deionized water and ethanol. In a typical synthesis, 2 mmol of $Ni(NO_3)_2{\cdot}6H_2O$, 4 mmol of $Co(NO_3)_2{\cdot}6H_2O$ and 24 mmol urea were dissolved into a mixed solution of 40 mL ethanol and 40 mL H_2O at room temperature to form a clear pink solution. The solution was transferred to a 30 mL Teflon-lined stainless-steel autoclave, into which a piece of nickel foam was immersed. The autoclave was sealed and maintained at 85 °C for 8 h and then cooled down to room temperature. The samples were taken out of solution and washed with deionized water and ethanol. After drying the sample at room temperature, samples were annealed at 350 °C for 4 h to obtain $NiCo_2O_4$/Ni foam. The same procedure was followed for the preparation of Co_3O_4 filamentous nanoarchitectures on Ni form without Ni precursor.

2.3. Electrochemical methods

Electrochemical measurements were performed in a three-electrode system using Bio-Logic VSP potentiostats with Co_3O_4 and $NiCo_2O_4$ filamentous nanoarchitectures on Ni foam as working electrode, Pt wire as counter electrode and Hg/HgO/1.0 M KOH as reference electrode. All measured potentials used for electrochemical measurements in this study have been reported versusthe reversible hydrogen electrode (RHE) and were converted using the equation

$$E_{(V\ vs.\ RHE)} = E_{(V\ vs.\ Hg/HgO)} + E_{(Hg/HgO)}\ (\text{reference}) + 0.0591\ V \times pH\ (\text{at } 25\ ^\circ C) \quad (1)$$

$E_{Hg/HgO}$ (reference, 1 M KOH) = 0.098 V vs. NHE at 25 °C

Electrochemical HMF oxidation experiments were conducted in 1 M KOH (pH 13.6) aqueous solution in the presence or absence of 5 mM HMF.

Electrochemically active surface area (ECSA) of the Co_3O_4 and $NiCo_2O_4$ filamentous nanoarchitectures on Ni foam can be determined by measuring the double layer charging current at different scan rates in 1 M KOH following here:

$$ECSA = C_{dl}/C_s \quad (2)$$

where C_s is the specific capacitance (0.040 m F/cm^2) in 1 M KOH solution. Here, the value of 0.040 m F/cm^2 was used based on previously reported metal oxide catalysts [23]. C_{dl} was calculated as a slop of the plot of capacitive current from a non-faradaic double-layer region against scan rate.

2.4. Characterization

The morphology and crystal structure as well as chemical composition of as-prepared Co_3O_4 and $NiCo_2O_4$ filamentous nanoarchitectures was examined with scanning electron microscope (SEM; cold emission scanning electron microscopy), transmission electron microscope (TEM) capable of a high-resolution transmission electron microscope (HRTEM) study, energy dispersive spectroscopy (EDS; Bruker quantax EDS) analysis and selected area electron diffraction (SAED; JEOL JEM-2100 F system operating at 200 kV). To determine the atomic binding structures and states in the samples were measured by X-ray photoelectron spectroscopy (XPS; K-alpha, Thermo UK) employing a monochromated Al Kα X-ray source. The in-situ XANES was measured at the 10C beam line of the Pohang Accelerator Laboratory (PAL) with 3-electrode electrochemical cell. Pt wire used as the counter electrode and Hg/HgO/1 M KOH electrode used as reference electrode with 1 M KOH (pH 13.6) aqueous solution in the presence of 5 mM HMF.

2.5. Catalytic testing

To analyze the concentration changes of HMF and its oxidation products in anolyte, 10 µl of solution during and after the reaction were taken from the cell and analyzed using HPLC (YL9100 chromatograph system with an ultraviolet-visible detector (YL9120) set at 265 nm). Sulfuric acid (5 mM) was used as the mobile phase in the isocratic mode. One hour of equilibration was required before each first injection. The flow rate was 0.5 ml/min at 65 °C. The samples and standards (10 µl) were injected directly onto a 300 mm × 7.7 mm Hi-Plex H column purchased from Agilent Technologies. The identification of the products and calculation of their concentrations were determined from calibration curves (correlation coefficient is 0.999) by applying a standard solution of known concentration. All data given in the report were an average of triplicate experiments.

The HMF conversion (%) and the selectivity of the oxidation products were calculated using the following equations;

$$\text{HMF conversion (\%)} = \frac{mol\ of\ HMF\ consumed}{mol\ of\ initial\ HMF} \times 100\% \quad (3)$$

$$Selectivity\ (\%) = \frac{mol\ of\ product}{mol\ of\ HMF\ converted} \times 100\% \quad (4)$$

The faradaic efficiency (FE) of FDCA product was calculated by

$$FE\ (\%) = \frac{mol\ of\ FDCA\ formed}{mol\ of\ total\ electrons\ passed/6} \times 100\% \quad (5)$$

3. Results and discussion

3.1. Characterization of CoO_4 and $NiCo_2O_4$ electrode

The synthesized Co_3O_4 and $NiCo_2O_4$ had filamentous nanoarchitectures on Ni foam in Fig. 1a and b. The high-magnification SEM image reveals that each filament of Co_3O_4 and $NiCo_2O_4$ is composed of 10–20 nm average diameter. The filamentous nanoarchitectures are composed of nanoparticles aligned in one dimension with diameters ranging from 5 to 15 nm. The nanoparticles are connected together to form a chain with one line of nanocrystals like pearls. These phenomena were confirmed by TEM results in Fig. 1. The Co_3O_4 and $NiCo_2O_4$ filamentous nanoarchitecture has a Co_3O_4 and $NiCo_2O_4$ spinel phases, respectively, which can be determined from HR-TEM images, filtered HR-TEM images and SAED patterns in Fig. 1c and d. Fig. 1c1 shows a clear filtered HR-TEM image of the sample which provides the detailed lattice fringes of Co_3O_4 filamentous nanoarchitectures. One set of fringes with a spacing of 0.28 nm are observed, which correspond to the (202) plane of cubic spinel Co_3O_4 [24]. It is also confirmed by the SAED pattern in Fig. 1c2. Also, filtered HR-TEM image of $NiCo_2O_4$ filamentous nanoarchitectures is shown in Fig. 1d1. The connected crystal structure have a lattice fringes (311) plane with d-spacing of 0.247 nm. The corresponding SAED pattern can be indexed to the spinel structure [25].

To further investigate the structure and composition of the samples, elemental mapping was carried out using an EDS instrument attached to a TEM. As shown Fig. S1, the results show that Co_3O_4 and $NiCo_2O_4$ consist of each element like Ni, Co and O.

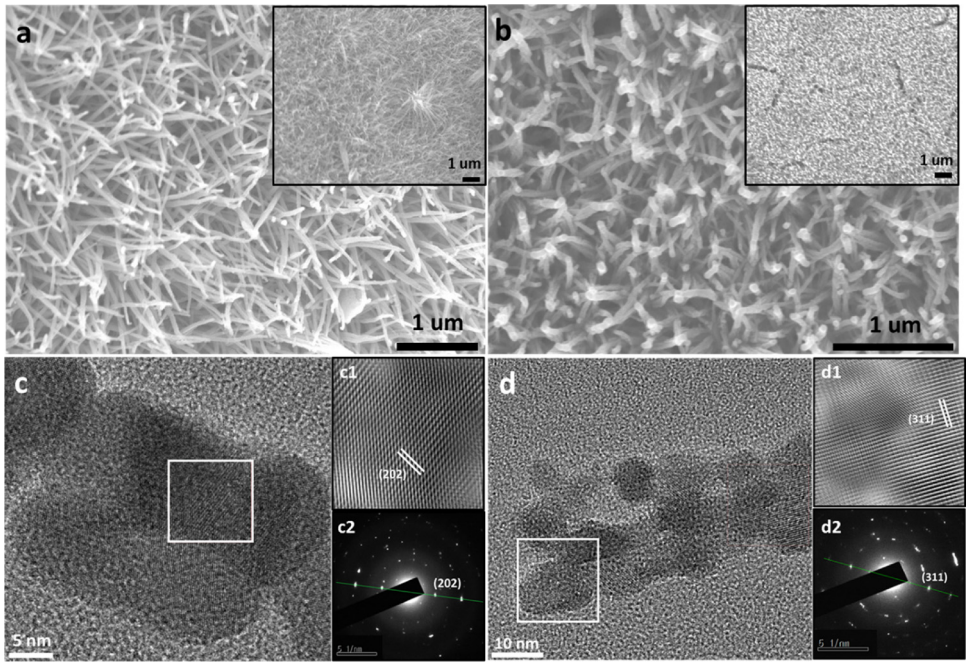

Fig. 1. SEM images (a, b; inset is low magnification image) and HR-TEM images (c, d) of Co_3O_4 and $NiCo_2O_4$ filamentous nanoarchitecture, respectively. (c1 and d1: refined HR-TEM images, c2 and d2: SAED patterns). The images in c1 and d1 are taken from the region marked with rectangle in c and d, respectively.

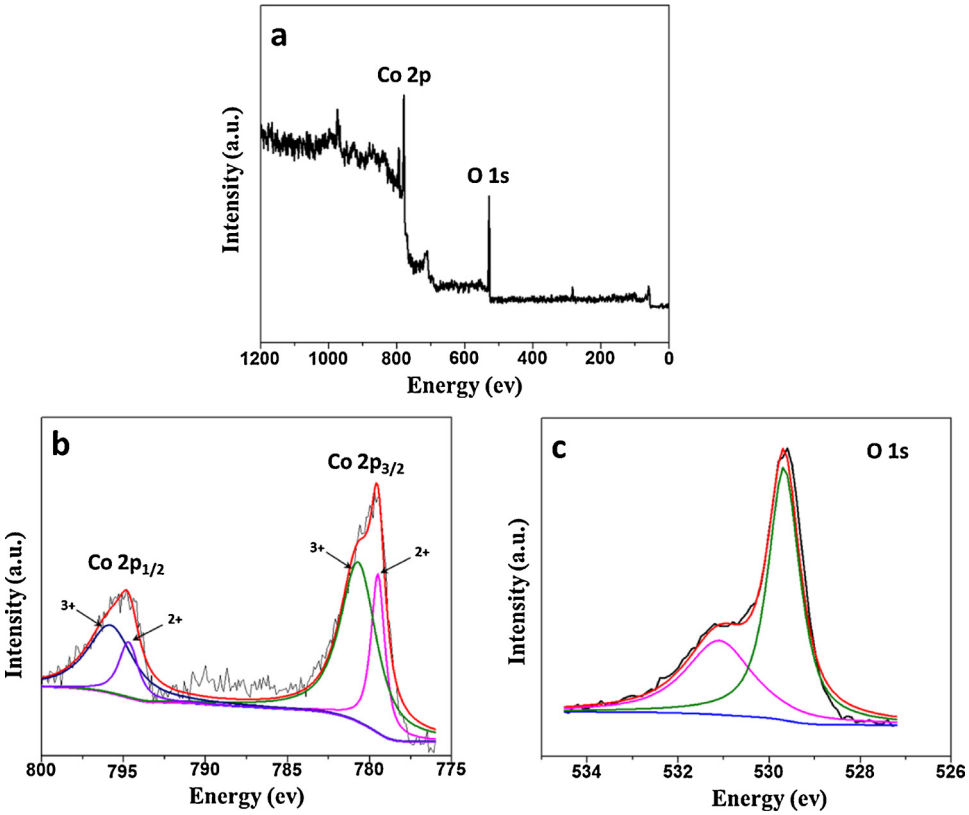

Fig. 2. XPS spectra of (a) survey spectrum, (b) Co 2p and (c) O 1s of Co_3O_4 filamentous nanoarchitectures.

Formation of the single phase in the Co_3O_4 and $NiCo_2O_4$ filamentous nanoarchitecture was confirmed from XPS spectra in Figs. 2 and 3. The full survey of Co_3O_4 filamentous nanoarchitecture is shown in Fig. 2a. The O1 s spectrum of Co_3O_4 showed two peaks at 529.6 eV and 531.2 eV, which is consistent with Co-O bonding in Co_3O_4 at 529.6 eV and a high number of defect sites with a low oxygen coordination in metal with small particles size at 531.2 eV in Fig. 2c [26–28]. The core level $Co2p_{3/2}$ in Co_3O_4 can be deconvoluted as two peaks with binding energies of 778.2 and 781.2 eV. Similarly, the core level $Co2p_{1/2}$ in Co_3O_4 can be deconvoluted as two peaks with the binding energies of 794.7 and 796.4 eV.

The peaks at binding energies of 778.2 and 794.7 eV can be assigned

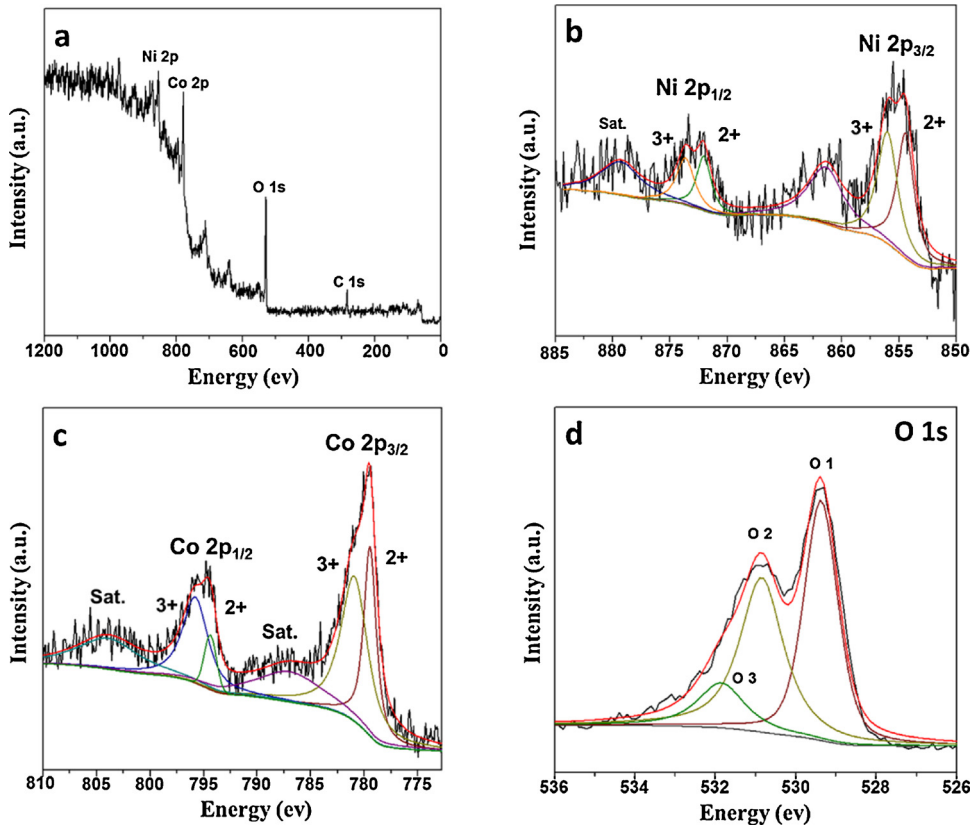

Fig. 3. XPS spectra of (a) survey spectrum, (b) Ni 2p, (c) Co 2p and (d) O 1s of $NiCo_2O_4$ filamentous nanoarchitectures.

to Co^{2+} of Co_3O_4 and the peaks at higher binding energies (781.2 and 796.4 eV) can be assigned to Co^{3+} of Co_3O_4 in Fig. 2b [29].

In the $NiCo_2O_4$ filamentous nanoarchitecture, the survey XPS spectrum is shown in Fig. 3a. In Ni $2p_{3/2}$ spectrum, the peaks can be deconvoluted to 854.6 eV and 855.9 eV, showing two spin-orbital doublets characteristic of Ni^{2+} and Ni^{3+} (Fig. S3b) [30]. Two spin-orbital doublets were also observed in Co $2p_{3/2}$ as Co^{2+} and Co^{3+} at 778.2 eV and 781.2 eV, respectively, in Fig. 3c [31]. The O 1 s spectrum can be deconvoluted to three different species of oxygen: typical metal-oxygen bonds at 529.4 eV (O1) [32], surface hydroxylated oxygen at 530.9 eV (O2) [33], and a high number of defect sites with low oxygen coordination in $NiCo_2O_4$ at 531.9 eV (O3) in Fig. 3d [34]. According to the TEM and XPS analysis results, Co_3O_4 and $NiCo_2O_4$ have the mixed state of Ni^{2+}, Ni^{3+}, Co^{2+}, and Co^{3+} spinel phase.

3.2. HMF oxidation performance

Since the oxygen evolution reaction (OER) competes with the electrocatalytic oxidation of HMF to FDCA in alkaline media, the OER reaction and HMF oxidation reaction were compared by linear sweep voltammetry (LSV). Without HMF, Co_3O_4 and $NiCo_2O_4$ filamentous nanoarchitecture showed catalytic onset potential of 1.47 and 1.42 V vs. RHE, respectively. Upon addition of 5 mM HMF, the catalytic onset potential shifted to ~1.2 V vs. RHE in both Co_3O_4 and $NiCo_2O_4$ while rapid current density increase was observed at ~1.43 V vs. RHE in $NiCo_2O_4$ in Fig. 4a. Over 1.43 V vs. RHE in $NiCo_2O_4$, the oxidation rate of HMF to FDCA is increased dramatically and reached 14.83 mA/cm^2 at 1.53 V vs. RHE, while the Co_3O_4 filamentous nanoarchitecture reached 8.17 mA/cm^2 at 1.53 V vs. RHE. Similarly, the calculated *Tafel* slope of $NiCo_2O_4$ decreased as 135.7 mV/dec, while the Co_3O_4 decreased 246.7 mV/dec, which means that lower potential was needed to increase the rate of HMF oxidation with the $NiCo_2O_4$ filamentous nanoarchitecture than with the Co_3O_4 filamentous nanoarchitecture in Fig. 4b.

Generally, the first reaction step of HMF oxidation to FDCA is the oxidation of HMF to HMFCA. HMFCA forms FFCA by oxidation. In the last step of HMF oxidation to FDCA, FFCA is oxidized to FDCA in Scheme S1. [35,36] To confirm that $NiCo_2O_4$ has higher efficiency than Co_3O_4 in all reactions from HMF to FDCA, LSV was measured with 5 mM of HMFCA solution and 5 mM of FFCA solution. With 5 mM of HMFCA solution, $NiCo_2O_4$ showed catalytic onset potential of 1.26 V vs. RHE with 11.99 mA/cm^2 current density at 1.50 V vs. RHE, while Co_3O_4 showed catalytic onset potential of 1.39 V vs. RHE with 6.69 mA/cm^2 current density at 1.55 V vs. RHE in Fig. S2a. With the 5 mM of FFCA solution, $NiCo_2O_4$ showed the catalytic onset potential of 1.26 V vs. RHE with 10.54 mA/cm^2 current density at 1.49 V vs. RHE, while Co_3O_4 showed catalytic onset potential 1.25 V vs. RHE with 7.08 mA/cm^2 current density at 1.51 V vs. RHE in Fig. S2b. These results confirmed that $NiCo_2O_4$ had higher HMF oxidation efficiency than Co_3O_4 during the entire HMF oxidation process.

To quantify and identify the oxidation products and to calculate the Faradaic efficiency (FE) of $NiCo_2O_4$ during the HMF oxidation reaction, the reaction was performed with applied bias potential of 1.5 V vs. RHE using a cell divided by a glass frit and 34.75 C of theoretical passed charge was applied in Fig. 5a. The anode, cathode, and overall reactions are summarized below;

$$\text{anode reaction: HMF} + 6\ OH^- \rightarrow \text{FDCA} + 4\ H_2O + 6\ e^- \quad (1)$$

$$\text{cathode reaction: } 6\ H_2O + 6\ e^- \rightarrow 3\ H_2 + 6\ OH^- \quad (2)$$

$$\text{overall reaction: HMF} + 2\ H_2O \rightarrow \text{FDCA} + 3\ H_2 \quad (3)$$

The conversion of HMF and yields of oxidation products with passed charge during HMF oxidation electrolysis is suggested in Fig. 5b. As increasing charge passed through $NiCo_2O_4$, HMF was oxidized to FDCA involves the oxidation of both alcohol and aldehyde group, with 99.63% of HMF converted to other oxidized products like HMFCA, DFF,

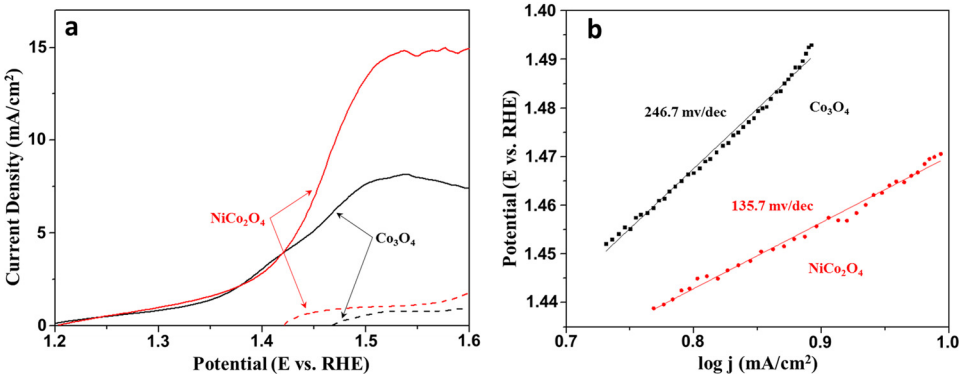

Fig. 4. (a) Linear sweep voltammetry (LSV) curves and (b) Tafel plots of Co_3O_4 and $NiCo_2O_4$ filamentous nanoarchitecture at 10 mV/s in 1 M KOH (pH 13.6) with (solid line) and without (dash line) 5 mM HMF. (black; Co_3O_4, red; $NiCo_2O_4$). (For interpretation of the references to colour in this figure legend, the reader is referred to the web version of this article.)

FFCA, and FDCA. The calculated HMF to FDCA conversion efficiency was 90.4%, with 90.8% FDCA selectivity and 87.5% faradaic efficiency.

The $NiCo_2O_4$ filamentous nanoarchitecture showed successful recyclability with repeated HMF oxidation cycles while maintaining high current density as HMF was added after the end of each electrolysis cycle in Fig. 5c. During three cycles of HMF to FDCA electrolysis, the $NiCo_2O_4$ filamentous nanoarchitecture retained the over 90% HMF conversion rate and still reached over 80% FDCA selectivity in Fig. 5d.

3.3. ECSA measurement

The electrochemical active surface area (ECSA) of Co_3O_4 and $NiCo_2O_4$ filamentous nanoarchitecture can be compared through the value of electrochemical double-layer capacitance (C_{dl}) because C_{dl} is proportional to ECSA.

$$\text{Electrochemical active surface area (ECSA)} = C_{dl}/C_s \quad (4)$$

where C_{dl} is the electrochemical double-layer capacitance of the catalytic surface and C_s is the specific capacitance of the sample or the capacitance of an atomically smooth planar surface (0.040 m F/cm^2) [23].

As shown in Fig. 6a and b, the cyclic voltammetry (CV) measurements were performed to investigate ECSA value of Co_3O_4 and $NiCo_2O_4$ electrode. The value of Cdl and ECSA are listed in Fig. 6d. As is shown in Fig. 6c, the C_{dl} values are obtained from slopes of fitting lines based on CV curves at different scan rate. It can be seen that the C_{dl} of $NiCo_2O_4$ is higher than Co_3O_4. According to Eq. (4), the ECSA values of $NiCo_2O_4$ is 6.75 cm^2, larger than Co_3O_4.

One of the reasons for the higher efficiency of HMF oxidation with the $NiCo_2O_4$ relative to the Co_3O_4 filamentous nanoarchitecture is difference in electrochemically active surface area. The larger ECSA value of $NiCo_2O_4$ was contributed to the higher efficiency of HMF oxidation reaction relative to Co_3O_4.

3.4. The role of Co^{3+} in Co_3O_4 and $NiCo_2O_4$ electrode for HMF oxidation

The XANES spectra of Co_3O_4 and $NiCo_2O_4$ filamentous nanoarchitecture before, during and after reaction shown in Fig. S3. As shown in Fig. 7, the coordination number (CN) change of Co atom during HMF oxidation reaction was analysed. White line energy shift (ΔE_0) in XANES spectra was discovered for Co_3O_4 and $NiCo_2O_4$ filamentous nanoarchitecture, having Co^{2+} and Co^{3+} mixed coordination state, similar with previous report [37]. Before the HMF oxidation reaction, the white line energy shift in Co_3O_4 filamentous nanoarchitecture was 19.6 eV, while the 19.4 eV in $NiCo_2O_4$ filamentous nanoarchitecture. In XANES spectra, lower white line energy shift means the lower CN of

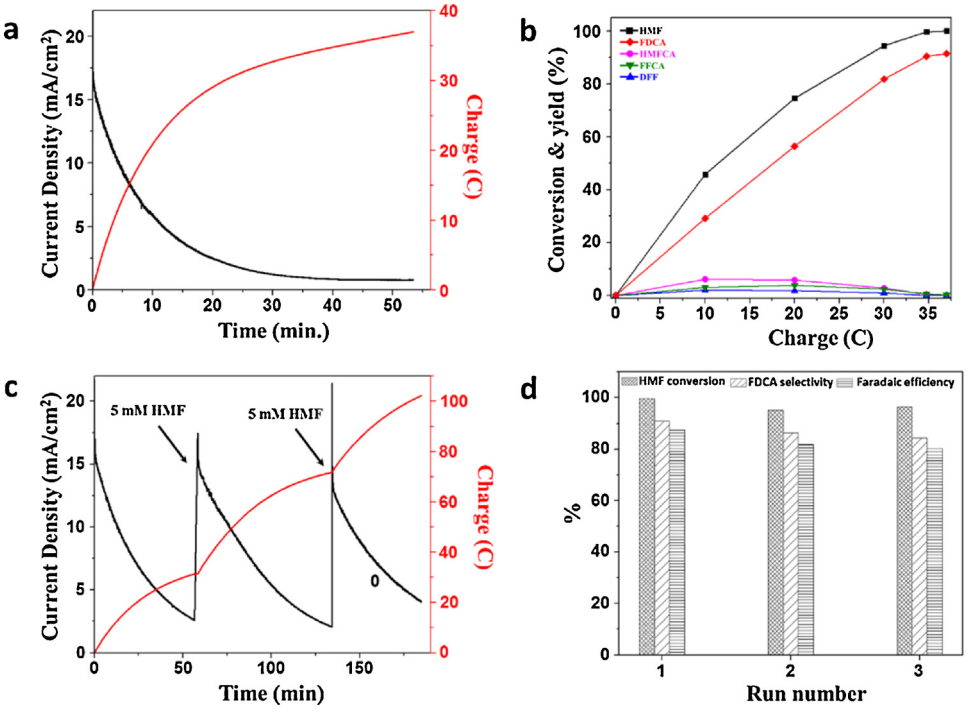

Fig. 5. (a) Chronoamperometric response curve, (b) conversion and yield of oxidation products over passed charge during electrolysis experiment, (c) current density and accumulated charge over the time with the addition of 5 mM HMF and (d) consecutive use of $NiCo_2O_4$ filamentous nanoarchitecture electrode at 1.5 V vs. RHE in 1 M KOH (pH 13.6) containing 5 mM HMF.

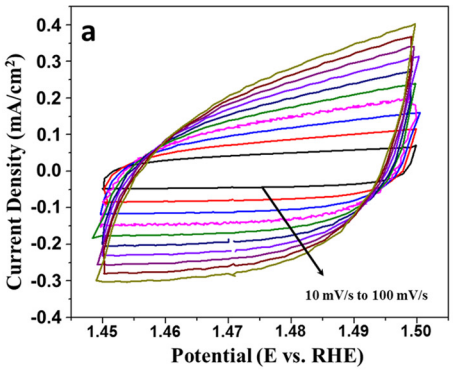

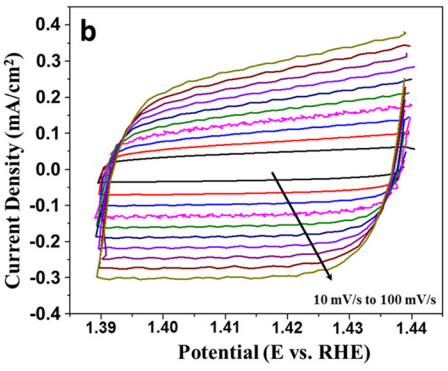

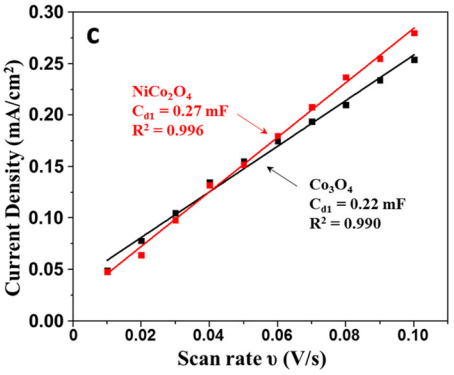

d

	Co_3O_4	$NiCo_2O_4$
C_{dl} (mF)	0.22	0.27
C_s (mF/cm²)	0.04	0.04
ECSA (cm²)	5.50	6.75

Fig. 6. Double-layer capacitance measurement for determining electrochemically active surface area. CVs on (a) Co_3O_4 and (b) $NiCo_2O_4$. (c) Current-scan rate curve. (d) Calculated ECSA. (black; Co_3O_4, red; $NiCo_2O_4$). (For interpretation of the references to colour in this figure legend, the reader is referred to the web version of this article.)

central Co atom. Both Co_3O_4 and $NiCo_2O_4$ have spinal structure with mixed state of tetrahedral Co (II) and octahedral Co (III), both results in energy shift of white line are similar within a form of Co_3O_4 [38]. However, Ni has the higher electronegativity than Co, some Co atoms in $NiCo_2O_4$ lost their coordination with oxygen due to nearby Ni atoms, which resulted in lower white line energy shifts in $NiCo_2O_4$ in Fig. 7(a).

These differences between Co_3O_4 and $NiCo_2O_4$ filamentous nanoarchitecture were dramatically shown during HMF oxidation reaction in Fig. 7(b). During the HMF oxidation reaction at 1.5 V vs. RHE, Co_3O_4 and $NiCo_2O_4$ showed ΔE_0 values of 19.5 eV and 19.2 eV, respectively. The lower ΔE_0 value means that CN of Co is decreased during reaction.

The decreased Co CN during HMF oxidation reaction means that the

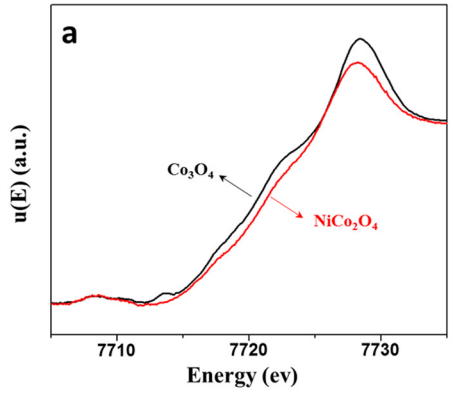

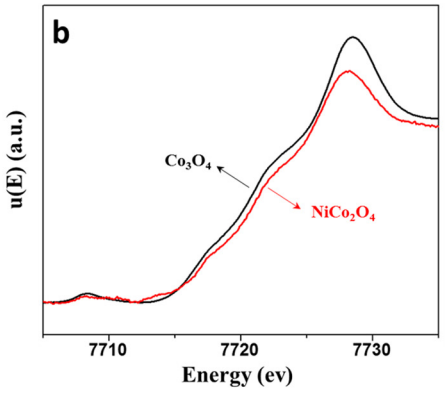

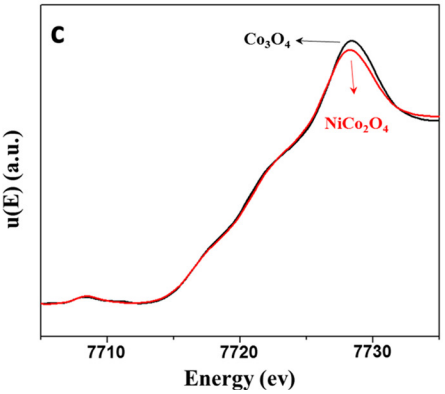

d

	ΔE_0	CN
Co_3O_4 Before reaction	19.6	2,3 mixed
Co_3O_4 During reaction	19.5	2,3 mixed
Co_3O_4 After reaction	19.6	2,3 mixed
$NiCo_2O_4$ Before reaction	19.4	2,3 mixed
$NiCo_2O_4$ During reaction	19.2	2,3 mixed
$NiCo_2O_4$ After reaction	19.4	2,3 mixed

Fig. 7. XANES spectra of Co_3O_4 and $NiCo_2O_4$ filament nanoarchitecture. (a) Before, (b) during and (c) after HMF oxidation reaction. (d) ΔE_0 and coordination number (CN) change of Co atom in Co_3O_4 and $NiCo_2O_4$ during HMF oxidation reaction. (Co_3O_4; black, $NiCo_2O_4$; red). (For interpretation of the references to colour in this figure legend, the reader is referred to the web version of this article.)

Co^{3+} species in Co_3O_4 and $NiCo_2O_4$ are participating in the oxidation of HMF by reduction of Co^{3+} to Co^{2+} under applied anodic potential [39]. This is supported by the XANES spectra after HMF oxidation reaction in Fig. 7(c). The decreased ΔE_0 values during HMF oxidation reaction are recovered as the original state (19.6 eV of ΔE_0 in Co_3O_4 and 19.4 eV of ΔE_0 in $NiCo_2O_4$) after the HMF oxidation reaction finished. The higher HMF oxidation efficiency of the $NiCo_2O_4$ than Co_3O_4 is derived from change of ΔE_0 between before and after reaction. The more decreased ΔE_0 value in $NiCo_2O_4$ during the HMF oxidation reaction (- 0.2 eV) compared with Co_3O_4 (- 0.1 eV) means that the Co^{3+} in $NiCo_2O_4$ filament nanoarchitecture is participating HMF oxidation reaction, reduced as the Co^{2+} rather than that of Co_3O_4, leading to the high HMF oxidation efficiency in $NiCo_2O_4$ filament nanoarchitecture.

4. Conclusion

In summary, we developed Co_3O_4 and $NiCo_2O_4$ filament nanoarchitecture with spinel structure to be used as electrochemical catalysts for HMF oxidation. The $NiCo_2O_4$ filamentous nanoarchitecture showed an enhanced HMF oxidation efficiency than Co_3O_4 with recording 99.6% HMF conversion efficiency and 90.8% selectivity on FDCA. Furthermore, the $NiCo_2O_4$ filamentous nanoarchitecture is successfully recycled within 3 cycles of HMF oxidation with maintaining over 80% FDCA conversion efficiency. The reason for the increased HMF conversion efficiency of $NiCo_2O_4$ compare to Co_3O_4 spinel structure, which was revealed by XPS and XANES analysis, is higher portion of reduced Co^{3+} to Co^{2+} under applied anodic potential in $NiCo_2O_4$ electrode becoming the active sites during the HMF oxidation reaction than Co_3O_4 electrode.

Acknowledgements

This work was supported by Korea Research Institute of Chemical Technology (KRICT) core project (SI1809 & KK1806). S.Y.H. acknowledges funding from the Ministry of Trade, Industry and Energy (MOTIE, Korea) through the Technology Innovation Program (10070150). We thanks to Dr. Min Kyu Kim, manager of the 10C beam line at Pohang Accelerator Laboratory (PAL), for helping with XANES measurements.

Appendix A. Supplementary data

Supplementary material related to this article can be found, in the online version, at doi:https://doi.org/10.1016/j.apcatb.2018.09.087.

References

[1] S. Chu, A. Majumdar, Nature 488 (2012) 294–303.
[2] P.C.A. Bruijnincx, B.M. Weckhuysen, Nat. Chem. 6 (2014) 1035–1036.
[3] H. Xiong, T.J. Schwartz, N.I. Andersen, J.A. Dumesic, A.K. Datye, Angew. Chem. Int. Ed. 54 (2015) 7939–7943.
[4] F. Xu, J. Sun, N.V.S.N.M. Konda, J. Shi, T. Dutta, C.D. Scown, B.A. Simmons, S. Singh, Energy Environ. Sci. 9 (2016) 1042–1049.
[5] I. Krivtsov, E.I. Garcia-Lopez, G. Marci, L. Palmisano, Z. Amghouz, J.R. Garcia, S. Ordonez, E. Díaz, Appl. Catal. B: Environ. 204 (2017) 430–439.
[6] E.F. Iliopoulou, S. Stefanidis, K. Kalogiannis, A. Delimitis, A. Lappas, K. Triantafyllidis, Appl. Catal. B: Environ. 127 (2012) 281–290.
[7] Q. Hou, M. Zhen, L. Liu, Y. Chen, F. Huang, S. Zhang, W. Li, M. Ju, Appl. Catal. B: Environ. 224 (2018) 183–193.
[8] S. Rajendran, R. Raghunathan, I. Hevus, R. Krishnan, A. Ugrinov, M.P. Sibi, D.C. Webster, J. Sivaguru, Angew. Chem. Int. Ed. 54 (2015) 1159–1163.
[9] A.H. Motagamwala, W. Won, C. Sener, D.M. Alonso, C.T. Maravelias, J.A. Dumesic, Sci. Adv. 4 (2018) 1–8.
[10] T. Pasini, M. Piccinini, M. Blosi, R. Bonelli, S. Albonetti, N. Dimitratos, J.A. Lopez-Sanchez, M. Sankar, Q. He, C.J. Kiely, G.J. Hutchings, F. Cavani, Green Chem. 13 (2011) 2091–2099.
[11] Y.Y. Gorbanev, S.K. Klitgaard, J.M. Woodley, C.H. Christensen, A. Riisager, ChemSusChem 2 (2009) 672–675.
[12] X. Wan, C. Zhou, J. Chen, W. Deng, Q. Zhang, Y. Yang, Y. Wang, ACS Catal. 4 (2014) 2175–2185.
[13] G. Yi, S.P. Teong, Y. Zhang, Green Chem. 18 (2016) 979–983.
[14] W. Gong, K. Zheng, P. Ji, RSC Adv. 7 (2017) 34776–34782.
[15] D.-H. Nam, B.J. Taitt, K.-S. Choi, ACS Catal. 8 (2018) 1197–1206.
[16] W.P. Dijkman, D.E. Groothuis, M.W. Fraaije, Angew. Chem. Int. Ed. 53 (2014) 6515–6518.
[17] G.D. Yadav, R.V. Sharma, Appl. Catal. B: Environ. 147 (2014) 293–301.
[18] F. Neaţu, R.S. Marin, M. Florea, N. Petrea, O.D. Pavel, V.I. Pârvulescu, Appl. Catal. B: Environ. 180 (2016) 751–757.
[19] O. Casanova, S. Iborra, A. Corma, ChemSusChem 2 (2009) 1138–1144.
[20] S.E. Davis, L.R. Houk, E.C. Tamargo, A.K. Datye, R.J. Davis, Catal. Today 160 (2011) 55–60.
[21] H. Ait Rass, N. Essayem, M. Besson, ChemSusChem 8 (2015) 1206–1217.
[22] H.G. Cha, K.-S. Choi, Nat. Chem. 7 (2015) 328.
[23] C.C.L. McCrory, S. Jung, J.C. Peters, T.F. Jaramillo, J. Am. Chem. Soc. 135 (2013) 16977–16987.
[24] X.-P. Fu, Q.-K. Shen, D. Shi, K. Wu, Z. Jin, X. Wang, R. Si, Q.-S. Song, C.-J. Jia, C.-H. Yan, Appl. Catal. B: Environ. 211 (2017) 176–187.
[25] F.F. Tao, J.-j. Shan, L. Nguyen, Z. Wang, S. Zhang, L. Zhang, Z. Wu, W. Huang, S. Zeng, P. Hu, Nat. Commun. 6 (2015) 7798.
[26] J. Zhang, M. Chen, L. Zhu, RSC Adv. 6 (2016) 758–768.
[27] L. Zhang, W. He, X. Xiang, Y. Li, F. Li, RSC Adv. 4 (2014) 43357–43365.
[28] Z. Ren, Z. Wu, W. Song, W. Xiao, Y. Guo, J. Ding, S.L. Suib, P.-X. Gao, Appl. Catal. B: Environ. 180 (2016) 150–160.
[29] X. Xiang, L. Zhang, H.I. Hima, F. Li, D.G. Evans, Appl. Clay Sci. 42 (2009) 405–409.
[30] J.G. Kim, D.L. Pugmire, D. Battaglia, M.A. Langell, Appl. Surf. Sci. 165 (2000) 70–84.
[31] B. Cui, H. Lin, Y.-z. Liu, J.-b. Li, P. Sun, X.-c. Zhao, C.-j. Liu, J. Phys. Chem. C 113 (2009) 14083–14087.
[32] T. Choudhury, S.O. Saied, J.L. Sullivan, A.M. Abbot, J. Phys. D: Appl. Phys. 22 (1989) 1185.
[33] Y.E. Roginskaya, O.V. Morozova, E.N. Lubnin, Y.E. Ulitina, G.V. Lopukhova, S. Trasatti, Langmuir 13 (1997) 4621–4627.
[34] V.M. Jiménez, A. Fernández, J.P. Espinós, A.R. González-Elipe, J. Electron. Spectrosc. Relat. Phenom. 71 (1995) 61–71.
[35] M.E. Zakrzewska, E. Bogel-Łukasik, R. Bogel-Łukasik, Chem. Rev. 111 (2011) 397–417.
[36] G. Lv, H. Wang, Y. Yang, T. Deng, C. Chen, Y. Zhu, X. Hou, ACS Catal. 5 (2015) 5636–5646.
[37] J. Wang, J. Zhou, Y. Hu, T. Regier, Energy Environ. Sci. 6 (2013) 926–934.
[38] N.N. Greenwood, A. Earnshaw, 26 – Cobalt, Rhodium and Iridium, Chemistry of the Elements, second edition, Butterworth-Heinemann, Oxford, 1997, pp. 1113–1143.
[39] V.R. Mate, M. Shirai, C.V. Rode, Catal. Commun. 33 (2013) 66–69.